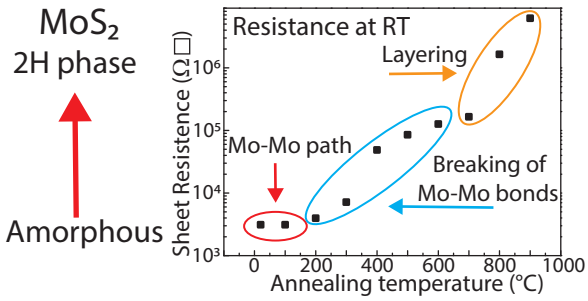

- Anomalous electrical conductivity change in MoS_2 during crystallization.
- A huge change in electrical resistance suggests the use of TMDC for data storage.
- Three separated resistance states can be used to encode data in three logic states.
- The low resistance amorphous state is due to a large quantity of Mo-Mo bonds.
- High resistance states arise from Mo-Mo bond disruption and crystallization.

Anomalous electrical conductivity change in MoS_2 during the transition from the amorphous to crystalline phase

Milos Krbal[a,*], Jan Prikryl[a], Igor Pis[b], Vit Prokop[a], Jhonatan Rodriguez Pereira[a], Alexander V. Kolobov[c]

[a] *Center of Materials and Nanotechnologies (CEMNAT), Faculty of Chemical Technology, University of Pardubice, Legions Square 565, 530 02 Pardubice, Czech Republic*
[b] *CNR-IOM, TASC Laboratory, 34149 Basovizza (TS), Italy*
[c] *Department of Physical Electronics, Institute of Physics, Herzen State Pedagogical University of Russia, 48 Moika Emb., St. Petersburg 191186, Russia*

Abstract

Transition metal dichalcogenides exhibit unique properties, which make them interesting for fundamental studies and for applications in many devices. Here, we report on anomalous electrical behaviour during the amorphous-to-crystal phase transition of MoS_2 . While crystallization typically results in an increase in conductivity, the situation in MoS_2 is opposite. Amorphous MoS_2 shows a sheet resistance of 3.2×10^3 $\Omega\square$ with the value remaining nearly constant until 200 °C, MoS_2 samples annealed above 200 °C exhibit an unexpected two-step *increase* in sheet resistance. The first abrupt increase takes place after annealing at temperatures between 300 and 400 °C while the second increase occurs after heating to 700 °C with typical sheet resistance values of 1.2×10^5 and 8×10^6 $\Omega\square$ after heating to 500 °C and 900 °C, respectively. Using a combination X-ray photoelectron spectroscopy and X-ray diffraction studies and ab-initio modeling, we argue that the large electrical conductivity observed in amorphous MoS_2 is associated with the existence of a large quantity of Mo-Mo homopolar bonds that exceed the percolation threshold. The dramatic increase in the sheet resistivity in the first step is accompanied by the formation of the

*Corresponding author
Email address: milos.krbal@upce.cz (Alexander V. Kolobov)

Mo-S bonds upon the disassociation of homopolar Mo-Mo bonds for a further increase in the sheet resistance upon annealing temperatures of 700 °C that can be attributed to the grain boundary formation during crystallization of MoS_2 into the 2H layered structure.

Keywords: `electrical conductivity, MoS2, structure, crystallization`

2016 MSC: 00-01, 99-00

---

1. Introduction

Due to their unique properties, both amorphous and crystalline chalcogenide materials have attracted attention for potential use in many fields such as infrared optics [1, 2], optoelectronics [3–5], nanophotonics [6, 7], solar cells [8–10], electrocatalytic hydrogen evolution [11–13], energy storage [12, 14, 15], data storage [16–18]. For example, data storage application takes advantage of the ultrafast reversible change in the optical and electrical properties of amorphous and crystalline phases induced by laser or electrical pulses, that are accompanied by a pronounced property contrast, which can serve to encode and store information [19]. In non-volatile memory devices, such as 3D XPoint [20] memory recently commercialized by Intel and Micron, the amorphous phase exhibits large electrical resistivity (RESET). The resistivity decreases by several orders of magnitude during the phase transition to the crystalline (SET) state. For the best performance, $Ge_2Sb_2Te_5$ [21] has been singled out as a prototypical phase-change material. A similar characteristic contrast (decrease) in resistivity upon crystallization has been observed for other phase change materials such as $(GeTe)_x - (Sb_2Te_3)_{1-x}$ tie-line compounds [22–24], $Ag_{6.0}In_{4.5}Sb_{60.8}Te_{28.7}$ [23, 25], Sb_2Te [26], $Ge_{0.15}Sb_{0.85}$ [27], In_2Se_3 [28] or $GeCu_2Te_3$ [29]. It should be noted that not only the above class of materials, but also metallic glasses [30] or even glassy carbon [31] exhibit a similar trend of showing a decrease in resistivity during the transition from the amorphous to the crystalline phase. This behavior can be considered typical for phase-change materials.

The recent discovery of an unusual reversible inverse resistance change in $CrGeTe_3$ [32], opposite to that of the often used $Ge_2Sb_2Te_5$, has opened a new path to engineer novel stable phase-change materials with desired properties. The origin of the low resistance RESET state in $CrGeTe_3$ was explained as being due to the formation of close-packed Cr clusters that led to carrier generation due to vacancy-induced defects. Subsequent disappearance of interconnected Cr-Cr clusters in the SET state was found to lead to a drastic increase in the resistivity, which resulted in the observed inverse resistance contrast.

Chromium belongs to Group VI of the Periodic Table, which also includes molybdenum and tungsten. These elements in combination with chalcogens form a widely studied class of materials today, the so-called Transition Metal Dichalcogenides (TMDCs) [4, 33] with the generic formula MX_2, where M represents a IV-VI transition metal atom and X is a chalcogen. As recently reported, similar to amorphous $CrGeTe_3$ [34], an as-deposited amorphous MoS_2 thin film contains a large number of homopolar Mo-Mo bonds [35], which can also form interconnected Mo-Mo paths and thus lead to a significant decrease in the electrical resistivity. Both amorphous phases - $CrGeTe_3$ and MoS_2 - crystallize into layered structures, which suggests that MoS_2 may also exhibit a similar unusual inverse conductive character.

To investigate further, we measured sheet resistance of MoS_2 in the as-deposited amorphous phase and during its gradual transformation into the stable 2H phase. We provide an explanation of the unusual behaviour in electrical conductivity using a combination of the sheet resistance values along with information on the structure of the as-deposited and individually annealed MoS_2 thin films obtained by X-ray photo-electron spectroscopy (XPS) and X-ray diffraction (XRD). The origin of the high conductivity of the as-deposited MoS_2 thin films is further corroborated by a model of "melt-quenched" (MQ) amorphous MoS_2 obtained via ab-initio molecular dynamics (AIMD) simulations.

2. Methodology

2.1. Experimental details

Amorphous MoS_2 films were deposited at room temperature using RF magnetron sputtering onto silica and silicon substrates. The thickness of the as-deposited films was about 50 nm. We performed depositions under the following conditions: 1 inch MoS_2 target, a distance between the target and sample holders was 12.2 cm, a background pressure was $1{\times}10^{-4}$ Pa, a forward power was 11 W and Ar pressure was 1.14 Pa. To prevent sample oxidation during crystallization, a–MoS_2 samples were placed into a clean quartz ampule which was subsequently evacuated to 10^{-3} Pa and sealed. Subsequent crystallization was performed in a furnace with a heating rate of 2 °C/ min. Samples were soaked at a given temperature in a range 100 to 900 °C for one hour and allowed to naturally cool down to room temperature.

The sheet resistance was measured using a Van der Pauw four probe setup equipped with a heating cell (THMSG 600). Measurements were performed over a temperature range 20 to 300 °C with a heating rate of 2 °C/ min. An Ar inert atmosphere was used to prevent sample oxidation. Drift in the sheet resistance for as-deposited MoS_2 were measured at 80, 140 and 180 °C with a heating rate of 50 °C/ min while maintaining the desired temperature for 6h.

The amorphous and crystalline states of MoS_2 were probed by X-ray diffraction using Cu K_α ($\lambda = 1.5406$ Å) X-ray source and a diffractometer (Empyrean Malvern Panalytical) operated in the 2-theta/omega mode in a Bragg-Brentano geometry.

Surface compositional analyses were carried out by X-ray photoelectron spectroscopy (XPS, ESCA2SR, Scienta-Omicron) using a monochromatized Al K_α (1486.7 eV) X-ray source. Binding energies were calibrated to the adventitious carbon peak at 284.8 eV. The spectra were fitted using Shirley-type background removal [36] and Voigt functions. S 2p and Mo 3d peak doublets separations, peak widths and intensity ratios were calibrated using a MoS_2 powder reference.

2.2. Computational details

The melt-quenched (MQ) amorphous phase of MoS_2 was generated via AIMD using the Vienna ab initio simulation package (VASP) [37]. Projector-augmented wave pseudopotentials that included the electron configurations $3s^2$ $3p^4$ and $4d^5$ $5s^1$ as valence states for S and Mo, respectively, were used. The PBE exchange-correlation functional [38] was used with a plane-wave basis with a cutoff energy of 260 eV. The initial 108 atom cell (the 2H phase containing 36 and 72 atoms of Mo and S, respectively) was randomized at 5000K for 10 ps to reach a molten phase. The temperature of the structure was subsequently decreased to 2200K over an additional 10 ps and maintained at this temperature for 10 ps to obtain an equilibrium state and then quenched to 200K over 10 ps. The crystallization of the MQ-MoS_2 was performed at 1800K for 200 ps.

3. Results and Discussion

The influence of the amorphous-to-crystal transition, in this case a so-called 3D-2D transition, on the electrical properties in MoS_2 thin films was thoroughly studied by electrical transport experiments. The MoS_2 thin films, which were annealed ex-situ over a range of temperatures from RT to 900 °C with a step of 100 °C, were investigated by sheet resistance measurements over the temperature range from RT to 300 °C with a step of 2 °C/min as shown in Fig. 1A. We found that the as-deposited amorphous MoS_2 thin film had a sheet resistance value of $3.2 \times 10^3\,\Omega\,\square$ at room temperature, which is several orders of magnitude lower that the value generally expected for amorphous sulfur-based solids [39] and conventional amorphous chalcogenides used for data storage [22, 24, 25, 40]. This value is even about one order of magnitude lower than the recently reported sheet resistance of as-deposited $CrGeTe_3$ thin film [32] and comparable with those of $GeCu_2Te_3$ [29] and $TiTe_2$ [41]. Upon heating to 300 °C, the sheet resistance of the as-deposited MoS_2 gradually decreased, indicating a semiconductor character, with no observed phase transition until

the final temperature point. Surprisingly, all ex-situ samples annealed above 200 °C showed an increased sheet resistance, which is anomalous behavior for amorphous chalcogenides excluding $CrGeTe_3$ [32]. We found that the overall electrical contrast between the as-deposited samples and samples annealed at 900 °C MoS_2 was roughly three and a half orders of magnitude at room temperature, which is comparable to conventional phase-change materials such as GeTe and $Ge_2Sb_2Te_5$. As can be seen in Fig. 1B, the electrical contrast change occurs in two steps, which are separated by a plateau that exhibits a gradual increase in sheet resistance. The first abrupt one order of magnitude increase in sheet resistance occurs between 300 and 400 °C while the second rapid two orders of magnitude increase occurred between 700 and 900 °C.

Unlike the conventional phase-change devices, two well defined annealing regimes result in large and reproducible electrical contrast between the low-resistant (amorphous), intermediate-resistant and high-resistant states; these states can be exploited to encode data in three logic states or so-called trits "0", "1" and "2". As a result, the use of a ternary system in multi-level data storage can serve to significantly increase storage density.

Typically, amorphous chalcogenide semiconductors undergo structural relaxation at elevated temperatures below their glass-transition temperature [42, 43], which is associated with an *increase* in the electrical resistance, so-called "resistance drift" [44]. This behavior is of special interest here because it cannot be linked to structural relaxation towards the crystalline phase, which would be expected to result in a *decrease* in resistivity. Fig. 1C shows the sheet resistance of as-deposited MoS_2 measured at three different temperatures for 6h, namely 80, 140 and 180 °C to examine the thermal stability of the amorphous low-resistance MoS_2 phase. We found that the resistance drift is thermally accelerated in a similar manner as observed in conventional $Ge_2Sb_2Te_5$ phase-change alloys [44] however, in the case of as-deposited MoS_2 , the structural relaxation results in a decrease in the electrical contrast between the low-resistance and intermediate-resistance states, a trend opposite to that of $Ge_2Sb_2Te_5$. The inset to Fig. 1C shows log-log plots of the sheet resistance increase with time.

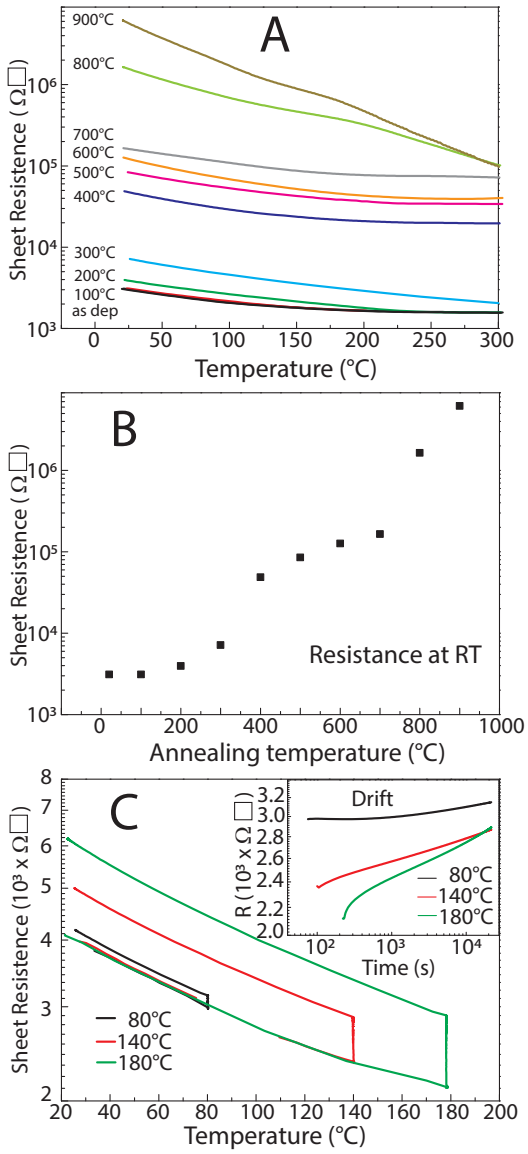

Figure 1: (Color online) (A) The temperature dependence of the sheet resistance over the temperature range from 20 to 300 °C of the as-deposited and annealed MoS_2 in the range of temperatures from 100 to 900 °C with step of 100 °C. (B) The evolution of the sheet resistance measured at 20 °C for as-deposited and annealed MoS_2 samples. (C) Drift in sheet resistance in as-deposited MoS_2 were measured at 80, 140 and 180 °C for 6h.

Thermal acceleration of the resistance drift can be determined from the slope of a linear function representing the rate constant with obtained values 0.018, 0.035 and 0.056 $\Omega\Box s^{-1}$ for 80, 140 and 180 °C, respectively .

An explanation of the observed anomalous inverse electrical conductivity between the as-deposited and crystallized MoS_2 thin films until 900 °C can be in principle divided into three parts, namely 1) the origin of the high conductivity of the as-deposited amorphous MoS_2 thin films, 2) the first abrupt increase in the sheet resistance between 300 and 400 °C and finally 3) the second rapid increase in the sheet resistance above 700 °C.

Recently, we have shown that as-deposited stoichiometric amorphous MoS_2 contains about 25% Mo-Mo homopolar bonds [35]. To unravel the role of these Mo-Mo bonds in the electric conductivity at the atomic level, we have employed a model of "melt-quenched" (MQ) amorphous MoS_2 obtained via AIMD simulations using the VASP code [37]. Fig. 2 shows the melt-quenched-MoS_2 phase, which was composed of 108 atoms in the simulation cell (36 Mo atoms and 72 S atoms). By careful analysis of the Mo-Mo bonds constrained using a bond length cutoff of 3.2 Å in the MQ model, we found that the Mo-Mo homopolar bonds form multiple conductive paths through the amorphous phase. Because Mo-Mo bonds have a metallic character, the formed clusters or conductive filaments significantly improve the electron transport through the amorphous MoS_2 phase. Thus, the electron conductivity in the amorphous MoS_2 phase is generally governed by percolation theory [45], where, in this case, the concentration of Mo-Mo bonds affects the overall conductivity.

To verify the above idea of the role of the Mo-Mo homopolar bond concentration on the sheet resistance, we performed XPS analyses of as-deposited and annealed MoS_2 over a range of temperatures from 300 to 900 °C as shown in Fig 3. A recent analysis of the Mo 3d core level for as-deposited amorphous MoS_2 revealed [35] a mixture of four doublets attributable to Mo(IV)-S in 1T' - like phase (magenta) containing Mo-Mo homopolar bonds with the binding energy, $E_B(3d_{5/2})$ = 228.8 eV [11, 46], Mo(IV)-S in 2H - like symmetry (light blue) with $E_B(3d_{5/2})$ = 229.3 eV [46], a weak signal attributable to Mo(VI)-O in

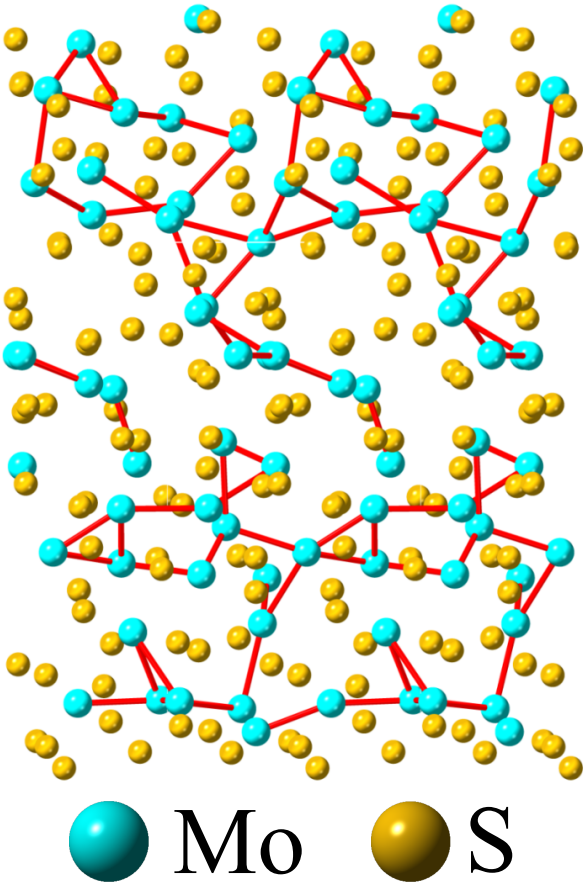

Figure 2: (Color online) The MQ-MoS_2 amorphous phase modeled via molecular dynamic using the VASP code. The red lines represent the formation of Mo-Mo paths. The bond length cutoff is 3.2 Å

.

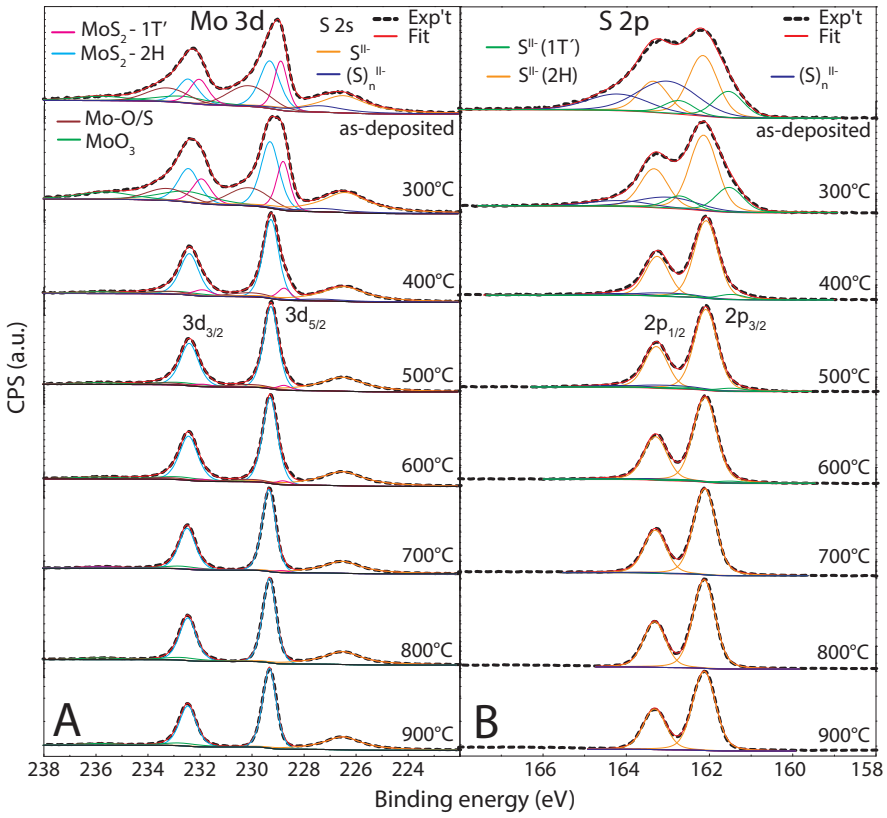

Figure 3: (Color online) XPS spectra (A) Mo 3d and (B) S 2p of the as-deposited and annealed MoS_2 in the range of temperatures from 300 to 900 °C.

MoO_3 (green) with $E_B(3d_{5/2})$ = 232.93 eV [47] and molybdenum oxo-sulphides Mo(IV)-O/S or Mo(V) (brown) with $E_B(3d_{5/2})$ = 230.3 eV [48, 49]. Satellites in as-deposited MoS_2 derived from final state screening effects could also contribute to the last component [50, 51]. Broad bands at E_B(2s) = 226.5 eV and E_B(2s) = 227.4 eV are attributable to S(II-) [11] and $(S)_n$(II-) 2s [11], respectively.

A detailed analysis of the Mo 3d core level (see Fig. 3A) disclosed that the first decrease of the intensity signal attributable to Mo(IV)-S in 1T' - like symmetry appeared at 300 °C followed by the significant transformation of this structural unit to Mo(IV)-S in 2H - like symmetry at 400 °C. With further increasing temperature, the contribution of the 1T' - like symmetry gradually decreases until 700 °C and above this temperature, the MoS_2 structure is exclusively formed by the Mo(IV)-S in 2H - like symmetry units, which are typical for the crystalline phase of MoS_2 [52]. The co-existence of both Mo(IV)-S structural units at different temperatures is better shown in Fig. 4A, where the 1T' / 2H MoS_2 ratio forms a characteristic sigmoid curve with a sudden sharp drop in value observed in the temperature range 300-400 °C, which is exactly the temperature range in which the sheet resistance abruptly increases. We can therefore conclude that the extinction of Mo-Mo homopolar bonds, associated with the transformation of 1T' - like symmetry into 2H-like symmetry units, plays a key role in the first abrupt increase in sheet resistance between 300 and 400 °C.

The S 2p XPS spectra exhibit a similar trend as shown in Fig. 3B. The main doublet with S $2p_{3/2}$ core level at 162.1 eV corresponds to 2H-MoS_2 and the second contribution shifted by -0.6 eV can be assigned to the 1T'-like phase [11, 53–55]. The ratio between these two S 2p components displays the same trend as Mo 3d (Fig. 4B). A third component with S $2p_{3/2}$ at 163 eV is necessary to obtain a good fit for the spectra corresponding to lower temperatures. This contribution is attributed to polysulphides $(S)_n$(-II)) with a variable number of sulfur atoms in the chain [56].

The subsequent sharp decrease in the $(S)_n$(-II)/S(-II) ratio at temperatures

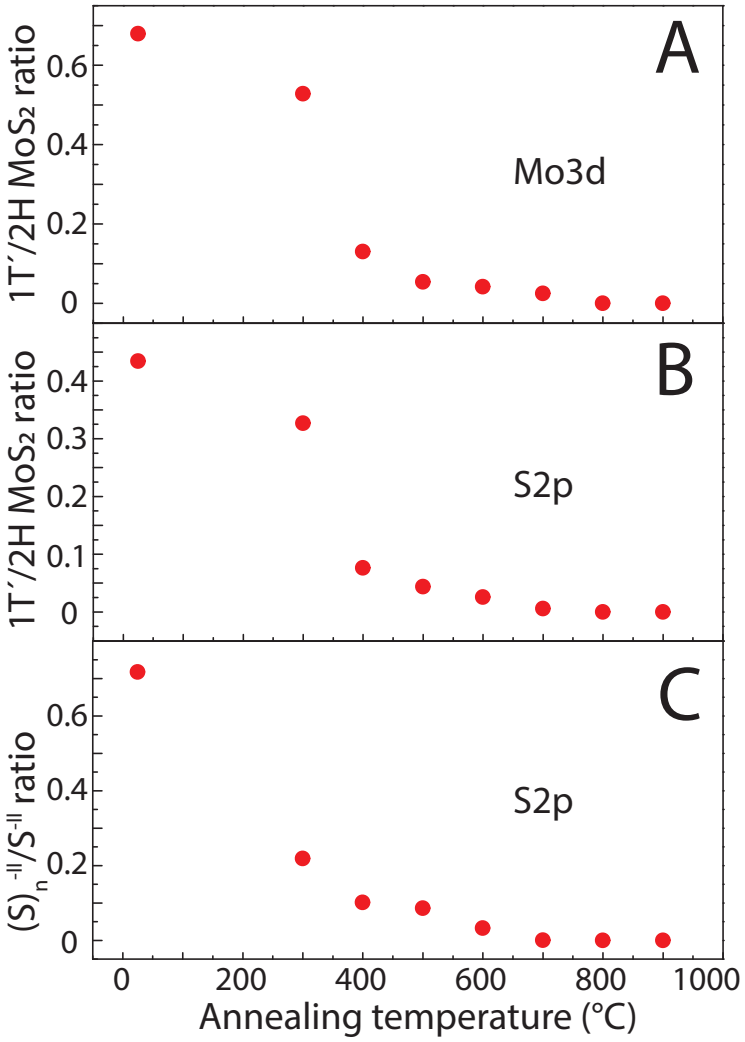

Figure 4: (Color online) Areal ratios of (A) Mo3d signals attributable to 1T' -like and 2H-like structural units and (B) S2p signals attributable to 1T' -like and (C) S 2p attributable to $(S)_n{}^{II-}$ and S^{II-} for the as-deposited and annealed MoS_2 in the range of temperatures from 300 to 900 °C.

above 200 °C is associated with the formation of heteropolar Mo-S bonds. The contribution of homopolar sulfur bonds in polysulfides linearly decreases with increasing temperature in the range of temperatures from 300 to 700 °C; above this temperature, all sulfur atoms are bonded solely to the Mo atoms and form heteropolar Mo-S bonds, as demonstrated in Fig. 4C.

The evolution of valence band spectra (VB) of amorphous MoS_2 upon crystallization is shown in Fig 5. The valence band of the as-deposited MoS_2 phase is formed by two broad bands in the range of binding energies 0 - 10 eV, which can be fitted by seven Gaussian peaks (see Fig. 5A). The VB spectrum of the as-deposited phase remains similar even for MoS_2 annealed until 300 °C. Above this temperature, the characteristic six major bands for the 2H MoS_2 phase appear as a consequence of the transformation of the 1T'-like to 2H-like structural units and subsequent crystallization as shown in Fig. 5B. One can see that the VB spectral shape is very similar for the temperature range from 400 to 600 °C, while the subsequent increase in intensity of all bands occurs for temperatures above 700 °C. We speculate that the latter phenomenon is associated with the second sharp increase in sheet resistance. Focusing on the VB edge (see Fig. 5C), the VB edge of amorphous MoS_2 is positioned at 0.3 eV. Upon annealing up to 900 °C, the VB edge is shifted to 1.1 eV with the largest change being measured between 300 and 400 °C. The shift of the VB edge in samples annealed above 400 °C is caused by the extinction of the first Gaussian band in VB of amorphous MoS_2 , which perfectly corresponds to the dissociation of homopolar Mo-Mo bonds, causing the first abrupt increase in the sheet resistance of MoS_2 thin films.

Because the annealed structure above 700 °C is exclusively composed of heteropolar Mo-S bonds, as shown in Fig. 4, the second sudden increase in sheet resistance cannot simply be explained by the change in bonding. Analysis of the XRD patterns shown in Fig. 6 demonstrates that MoS_2 thin films appear amorphous even after annealing at 600 °C. Above this temperature, a broad single reflection peak at about 2θ =13.9 deg emerges from the amorphous background across the whole 2θ range from 5 to 60 deg. The reflection peak is a

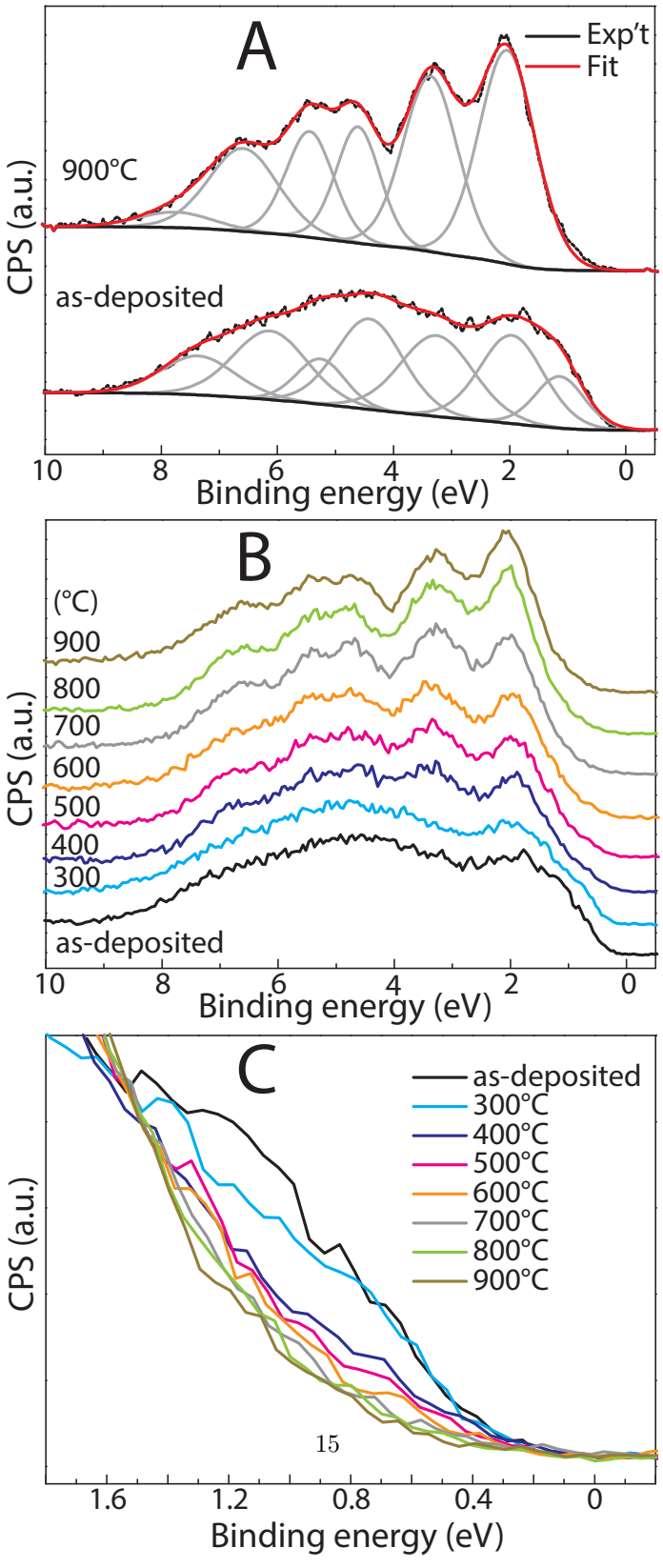

Figure 5: (Color online) The valance bands of as-deposited and annealed MoS_2 for temperatures from 300 to 900 °C.

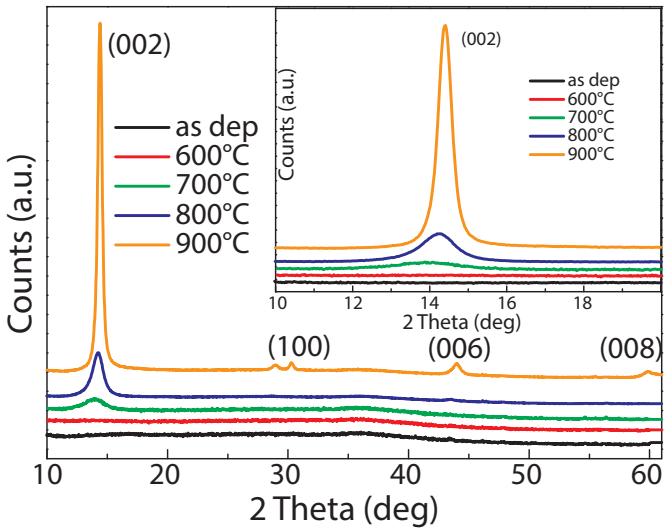

Figure 6: (Color online) X-ray diffraction patterns of the as-deposited and crystallized MoS_2 in the range of temperatures from 600 to 900 °C with a step of 100 °C.

good fit to the most intensive reflection peak along the (002) crystallographic plane, which indicates that the amorphous MoS_2 begins to crystallize in the 2H-MoS_2 layered phase. With increasing temperature from 700 to 900 °C, the Bragg reflection peak along the (002) crystallographic plane increases in intensity and at the same time reduces the full width at half maximum from 2.03 to 0.42 deg which unequivocally demonstrates an increase in crystal size along the c-axis. In addition, the peak position slightly shifts from 2θ =13.9 deg to 2θ =14.41 deg which can be related to a change in distance between S-Mo-S triplets. The XRD pattern shown in Fig. 6 for the MoS_2 sample annealed at 900 °C is sufficiently sharp to identify easily additional Bragg reflection lines along the (006) and (008) crystallographic planes which characterize the ordering of the two-dimensional layers into a well-crystallized multilayer of MoS_2 with a strong preferential crystal growth of the 2H-MoS_2 phase with out-of-plane c-axis orientation [52].

The consequence of the amorphous to crystal transformation is the formation of crystal grains and boundaries between them. In principle, the electrical con-

ductivity in polycrystalline materials is the sum of the conductivity through the crystals and across the grain boundaries, which are usually orders of magnitude more resistant than crystal interiors [57]. We believe that the grain boundaries hinder the charge transport among crystal grains of MoS_2 and this effect should be considered as the key factor of the second abrupt increase in sheet resistance. A recent report on a charge carrier mobility in mono-layered MoS_2 can provide alternative explanation [58]. The authors found that the charge carrier mobility is sensitive to sulfur vacancies, which act as scattering centers and can thus be responsible for its decrease by two orders of magnitude when the sulfur vacancy concentration is increased from 0.1 to 3%. Since such a small shift in composition determined by XPS is at the level of fitting errors, it is also necessary to take into account this contribution to the overall increase in the sheet resistance of MoS_2 layers annealed above 700 °C.

4. Conclusion

In conclusion, through a combination of experimental and theoretical studies, we demonstrated - and provided an explanation for - an anomalous inverse electrical conductivity change en route to the formation of the crystalline phase upon annealing of as-deposited amorphous MoS_2 films. Namely, we found that the high conductivity of as-deposited amorphous MoS_2 thin films is due to a high concentration of homopolar Mo-Mo bonds that form conductive percolation paths or clusters through the amorphous phase. The first abrupt increase in sheet resistance by one order of magnitude between 300 and 400 °C is attributable to the dissociation of the homopolar Mo-Mo bonds accompanied by the transformation of 1T' - like symmetry local building units into 2H-like symmetry units. Finally, we attribute the origin of the second rapid increase in the sheet resistance by two orders of magnitude starting from 700 °C to the gradual formation of grain boundaries that may hinder the charge transport among crystals of MoS_2 . The three-order change in electrical resistance suggests that TMDC thin films can be used for phase-change storage devices.

5. Data availability

The datasets generated during and/or analysed during the current study are available from the corresponding author on reasonable request.

6. Declaration of Competing Interest

The authors declare that there are no competing interests.

7. Acknowledgment

This work was supported by the Czech Science Foundation (19-17997S), The Ministry of Education, Youth and Sports (LM2018103) and the Russian Foundation for Basic Research (19-07-00353). I.P. acknowledge funding from the EUROFEL project (RoadMap Esfri).

References

[1] J.-B. Dory, C. Castro-Chavarria, A. Verdy, J.-B. Jager, M. Bernard, C. Sabbione, M. Tessaire, J.-M. Fdli, A. Coillet, B. Cluzel, P. Noe, Ge-Sb-S-Se-Te amorphous chalcogenide thin films towards on-chip nonlinear photonic devices, Sci Rep 10 (2020) 11894. doi:10.1038/s41598-020-67377-9.

[2] H. N. S. Krishnamoorthy, G. Adamo, J. Yin, V. Savinov, N. I. Zheludev, C. Soci, Infrared dielectric metamaterials from high refractive index chalcogenides, Nature Communications 11 (1) (2020) 1692.
URL https://doi.org/10.1038/s41467-020-15444-0

[3] Q. H. Wang, K. Kalantar-Zadeh, A. Kis, J. N. Coleman, M. S. Strano, Electronics and optoelectronics of two-dimensional transition metal dichalcogenides, Nat Nanotechnol. 7 (11) (2012) 699–712. doi:10.1038/nnano.2012.193.

[4] A. V. Kolobov, J. Tominaga, Two-dimensional Transition-Metal Dichalcogenides, Springer Series in Materials Science, Springer International Publishing AG, 2016.

[5] J.-W. Qiao, M.-S. Niu, Z.-C. Wen, X.-K. Yang, Z.-H. Chen, Y.-X. Wang, L. Feng, W. Qin, X.-T. Hao, Efficient photoluminescence enhancement and tunable photocarrier transfer in vertical 2d organic–inorganic heterostructure by energy funneling, 2D Materials 8 (2) (2021) 025026. doi:10.1088/2053-1583/abdf6b.
URL https://doi.org/10.1088/2053-1583/abdf6b

[6] S. Abdollahramezani, O. Hemmatyar, H. Taghinejad, A. Krasnok, Y. Kiarashinejad, M. Zandehshahvar, A. Al?, A. Adibi, Tunable nanophotonics enabled by chalcogenide phase-change materials, Nanophotonics 9 (5) (2020) 1189–1241. doi:doi:10.1515/nanoph-2020-0039.
URL https://doi.org/10.1515/nanoph-2020-0039

[7] B. Gerislioglu, G. Bakan, R. Ahuja, J. Adam, Y. K. Mishra, A. Ahmadivan, The role of $Ge_2Sb_2Te_5$ in enhancing the performance of functional plasmonic devices, Mater. Today Phys. 12 (2020) 100178. doi:10.1016/j.mtphys.2020.100178.

[8] M. Buscema, J. O. Island, D. J. Groenendijk, S. I. Blanter, G. A. Steele, H. S. J. van der Zant, A. Castellanos-Gomez, Photocurrent generation with two-dimensional van der waals semiconductors, Chem Soc Rev 44 (2015) 3691. doi:10.1039/c5cs00106d.

[9] M. Krbal, J. Prikryl, R. Zazpe, H. Sopha, J. M. Macak, Cds-coated TiO_2 nanotube layers: downscaling tube diameter towards efficient heterostructured photoelectrochemical conversion, Nanoscale 9 (2017) 7755–7759. doi:10.1039/C7NR02841E.
URL http://dx.doi.org/10.1039/C7NR02841E

[10] H. Lei, J. Chen, Z. Tan, G. Fang, Review of recent progress

in antimony chalcogenide-based solar cells: materials and devices, Solar RRL 3 (6) (2019) 1900026. arXiv:https://onlinelibrary.wiley.com/doi/pdf/10.1002/solr.201900026, doi:https://doi.org/10.1002/solr.201900026.
URL https://onlinelibrary.wiley.com/doi/abs/10.1002/solr.201900026

[11] J. Xie, H. Zhang, S. Li, R. Wang, X. Sun, M. Zhou, J. Zhou, X. Wen, D. Lou, Y. Xie, Defect-rich MoS_2 ultrathin nanosheets with additional active edge sites for enhanced electrocatalytic hydrogen evolution, Adv. Mater. 25 (2013) 5807–5813. doi:10.1002/adma.201302685.

[12] A. Eftekhari, Molybdenum diselenide ($MoSe_2$) for energy storage, catalysis, and optoelectronics, Appl. Mater. Today 8 (2017) 1–17. doi:10.1016/j.apmt.2017.01.006.

[13] J. McAllister, N. A. G. Bandeira, J. C. McGlynn, A. Y. Ganin, Y.-F. Song, C. Bo, H. N. Miras, Tuning and mechanistic insights of metal chalcogenide molecular catalysts for the hydrogen-evolution reaction, Nature Communications 10 (1) (2019) 370.
URL https://doi.org/10.1038/s41467-018-08208-4

[14] T. Wang, S. Chen, H. Pang, H. Xue, Y. Yu, MoS_2-based nanocomposites for electrochemical energy storage, Adv. Sci 4 (2) (2017) 1600289. doi:10.1002/advs.201600289.

[15] Q. Peng, F. Ling, H. Yang, P. Duan, R. Xu, Q. Wang, Y. Yu, Boosting potassium storage performance via construction of $NbSe_2$based misfit layered chalcogenides, Energy Storage Materials 39 (2021) 265–270. doi:https://doi.org/10.1016/j.ensm.2021.04.032.
URL https://www.sciencedirect.com/science/article/pii/S2405829721001719

[16] A. V. Kolobov, M. Krbal, P. Fons, J. Tominaga, Distortion-triggered loss

of long-range order in solids with bonding energy hierarchy, Nature Chem. 3 (2011) 311–316. doi:10.1038/nchem.1007.

[17] D. K. Loke, J. M. Skelton, T. H. Lee, R. Zhao, T.-C. Chong, S. R. Elliott, Ultrafast nanoscale phase-change memory enabled by single-pulse conditioning, ACS Appl. Mater. Interfaces 10 (49) (2018) 41855–41860. doi:10.1021/acsami.8b16033.
URL https://doi.org/10.1021/acsami.8b16033

[18] W. Zhang, R. Mazzarello, M. Wuttig, E. Ma, Designing crystallization in phase-change materials for universal memory and neuro-inspired computing, Nat Rev Mater 4 (2019) 150–168. doi:10.1038/s41578-018-0076-x.

[19] M. Wuttig, N. Yamada, Phase-change materials for rewriteable data storage, Nature Materials 6 (11) (2007) 824–832.
URL https://doi.org/10.1038/nmat2009

[20] F. T. Hady, A. Foong, B. Veal, D. Williams, Platform storage performance with 3d xpoint technology, Proc. IEEE 105 (9) (2017) 1822 – 1833. doi:10.1109/JPROC.2017.2731776.

[21] N. Yamada, E. Ohno, K. Nishiuchi, N. Akahira, M. Takao, Rapid–phase transitions of $GeTe - Sb_2Te_3$ pseudobinary amorphous thin films for an optical disk memory, Journal of Applied Physics 69 (5) (1991) 2849–2856. doi:10.1063/1.348620.
URL https://doi.org/10.1063/1.348620

[22] T. Siegrist, P. Jost, H. Volker, M. Woda, P. Merkelbach, C. Schlockermann, M. Wuttig, Disorder-induced localization in crystalline phase-change materials, Nature Materials 10 (3) (2011) 202–208. doi:10.1038/nmat2934.
URL https://doi.org/10.1038/nmat2934

[23] N. Saxena, C. Persch, M. Wuttig, A. Manivannan, Exploring ultrafast threshold switching in In_3SbTe_2phase change memory devices, Scientific

Reports 9 (1) (2019) 19251.
URL https://doi.org/10.1038/s41598-019-55874-5

[24] K. Ding, B. Chen, Y. Chen, J. Wang, X. Shen, F. Rao, Recipe for ultrafast and persistent phase-change memory materials, NPG Asia Materials 12 (1) (2020) 63. doi:10.1038/s41427-020-00246-z.
URL https://doi.org/10.1038/s41427-020-00246-z

[25] D. Kim, T. S. Jung, H. Park, W. Yang, J. Han, S. Hwang, K. I. Sim, Y.-K. Kwon, J. H. Kim, M.-H. Cho, Phase-change mechanism and role of each element in Ag-In-Sb-Te: Chemical bond evolution, Applied Surface Science 544 (2021) 148838.
URL https://www.sciencedirect.com/science/article/pii/S0169433220335972

[26] X. Shen, G. Wang, R. P. Wang, S. Dai, L. Wu, Y. Chen, T. Xu, Q. Nie, Enhanced thermal stability and electrical behavior of Zn-doped Sb_2Te films for phase change memory application, Appl. Phys. Lett. 102 (13) (2013) 131902. doi:10.1063/1.4799370.
URL https://doi.org/10.1063/1.4799370

[27] Y. Gu, T. Zhang, Z. Song, Y. Liu, B. Liu, S. Feng, Characterization of the properties for phase-change material GeSb, Applied Physics A 99 (1) (2010) 205–209.
URL https://doi.org/10.1007/s00339-009-5498-2

[28] H. Lee, D.-H. Kang, L. Tran, Indium selenide (In_2Se_3) thin film for phase-change memory, Materials Science and Engineering: B 119 (2) (2005) 196–201.
URL https://www.sciencedirect.com/science/article/pii/S092151070500156X

[29] A. El-Denglawey, M. M. Makhlouf, M. Dongol, The effect of thickness on the structural and optical properties of nano Ge-Te-Cu films, Results in

Physics 10 (2018) 714–720.
URL https://www.sciencedirect.com/science/article/pii/S2211379718308593

[30] C. Suryanarayana, A. Inoue, Metallic Glasses, Ullmann′s Encyclopedia of Industrial Chemistry, 2012, Ch. Electrical Resistivity, p. 24. doi:10.1002/14356007.a16_335.pub2.

[31] M. Yari, M. Larijani, A. Afshar, M. Eshghabadi, A. Shokouhy, Physical properties of sputtered amorphous carbon coating, Journal of Alloys and Compounds 513 (2012) 135–138. doi:https://doi.org/10.1016/j.jallcom.2011.10.006.
URL https://www.sciencedirect.com/science/article/pii/S0925838811019608

[32] S. Hatayama, Y. Shuang, P. Fons, Y. Saito, A. V. Kolobov, K. Kobayashi, S. Shindo, D. Ando, Y. Sutou, Cr-triggered local structural change in $Cr_2Ge_2Te_6$ phase change material, ACS Appl. Mater. Interface 11 (2019) 43320–43329. doi:10.1021/acsami.9b11535.

[33] S. Manzeli, D. Ovchinnikov, D. Pasquier, O. V. Yazyev, A. Kis, 2D transition metal dichalcogenides, Nature Reviews Materials 2 (8) (2017) 17033.
URL https://doi.org/10.1038/natrevmats.2017.33

[34] Y. Saito, S. Hatayama, Y. Shuang, P. Fons, A. V. Kolobov, Y. Sutou, Dimensional transformation of chemical bonding during crystallization in the layered chalcogenide material, Sci. Rep.doi:10.1038/s41598-020-80301-5.

[35] M. Krbal, V. Prokop, A. A. Kononov, J. Rodriguez-Pereira, J. Mistrik, A. V. Kolobov, P. Fons, Y. Saito, S. Hatayama, Y. Shuang, Y. Sutou, S. A. Rozhkov, J. R. Stellhorn, S. Hayakawa, I. Pis, F. Bondino, Amorphous-to-crystal transition in quasi two-dimensional MoS_2: Theory and experiment.

[36] D. A. Shirley, High-resolution x-ray photoemission spectrum of the valence bands of gold, Phys. Rev. B 5 (1972) 4709–4714. doi:10.1103/PhysRevB.5.4709.
URL https://link.aps.org/doi/10.1103/PhysRevB.5.4709

[37] G. Kresse, J. Hafner, Ab initio molecular dynamics for liquid metals, Phys. Rev. B 47 (1993) 558(R). doi:10.1103/PhysRevB.47.558.

[38] J. P. Perdew, K. Burke, M. Ernzerhof, Generalized gradientapproximation made simple, Phys. Rev. Lett. 77 (1996) 3865–3868. doi:10.1103/PhysRevLett.77.3865.

[39] E. R. Shaaban, M. Y. Hassaan, M. G. Moustafa, A. Qasem, E. S. Yousef, Sheet resistance temperature dependence, thermal and electrical analysis of $As_{40}S_{60} - xSex$ thin films, Applied Physica A 126 (2020) 34. doi:10.1007/s00339-019-3217-1.

[40] G. Wang, Y. Zhang, A. Lotnyk, H. Shi, C. Chen, High thermoelectric performance in znsb-snte pseudo-binary materials, Scripta Materialia 194 (2021) 113670. doi:10.1016/j.scriptamat.2020.113670.
URL https://www.sciencedirect.com/science/article/pii/S1359646220307922

[41] K. Ding, F. Rao, S. Lv, Y. Cheng, L. Wu, Z. Song, Low-energy amorphization of $Ti_1Sb_2Te_5$ phase change alloy induced by $TiTe_2$ nano-lamellae, Scientific Reports 6 (1) (2016) 30645.
URL https://doi.org/10.1038/srep30645

[42] M. M. Imran, A. F. Al-Shawabkeh, Structural relaxation due to sub-tg annealing of $Se_{98}In_{1.5}Sn_{0.5}$ chalcogenide glass, Journal of Alloys and Compounds 500 (2) (2010) 237–240. doi:https://doi.org/10.1016/j.jallcom.2010.04.017.
URL https://www.sciencedirect.com/science/article/pii/S092583881000808X

[43] A. M. Abd-Elnaiem, G. Abbady, A thermal analysis study of melt-quenched Zn_5Se_{95} chalcogenide glass, Journal of Alloys and Compounds 818 (2020) 152880. doi:https://doi.org/10.1016/j.jallcom.2019.152880.
URL https://www.sciencedirect.com/science/article/pii/S092583881934126X

[44] M. Boniardi, D. Ielmini, Physical origin of the resistance drift exponent in amorphous phase change materials, Appl. Phys. Lett. 98 (2011) 243506. doi:doi.org/10.1063/1.3599559.

[45] S. Kirkpatrick, Percolation and conduction, Rev. Mod. Phys. 45 (1973) 574–588. doi:10.1103/RevModPhys.45.574.
URL https://link.aps.org/doi/10.1103/RevModPhys.45.574

[46] A. Mondal, A. Paul, D. N. Srivastava, A. B. Panda, Defect- and phase-induced acceleration of electrocatalytic hydrogen production by ultrathin and small MoS_2-decorated rGO sheets, ACS Appl. Nano Mater. 1 (9) (2018) 4622–4632. doi:10.1021/acsanm.8b00914.

[47] T. H. Fleisch, G. J. Mains, An XPS study of the UV reduction and photochromism of MoO_3 and WO_3, J. Chem. Phys. 76 (1982) 780. doi:10.1063/1.443047.

[48] A. D. Gandubert, C. Legens, D. Guillaume, E. Payen, X-ray photoelectron spectroscopy surfacequantification of sulfided CoMoP catalysts. relationbetween activity and promoted sites. part ii: Influenceof the sulfidation temperature, Surf. Interface Anal. 38 (2006) 206–209. doi:10.1002/sia.2249.

[49] C.-H. Lin, C.-H. Tsai, F.-G. Tseng, Y.-Y. Yu, H.-C. Wu, C.-K. Hsieh, Low-temperature thermally reduced molybdenum disulfide as a Pt-free counter electrode for dye-sensitized solar cells, Nanoscale Research Letters 10 (1) (2015) 446.
URL https://doi.org/10.1186/s11671-015-1156-0

[50] D. Pariari, R. M. Varma, M. N. Nair, P. Zeller, M. Amati, L. Gregoratti, K. K. Nanda, D. Sarma, On the origin of metallicity and stability of the metastable phase in chemically exfoliated MoS_2, Appl. Mater. Today 19 (2020) 100544. doi:10.1016/j.apmt.2019.100544.

[51] D. O. Scanlon, G. W. Watson, D. J. Payne, G. R. Atkinson, R. G. Egdell, D. S. L. Law, Theoretical and experimental study of the electronic structures of MoO_3 and MoO_2, J. Phys. Chem. C 114 (10) (2010) 4636–4645. doi:10.1021/jp9093172.

[52] M. S. Whittingham, F. R. Gamble Jr., The lithium intercalates of the transition metal dichalcogenides, Mat. Res. Bull. 10 (1975) 363–372. doi:10.1016/0025-5408(75)90006-9.

[53] G. Eda, H. Yamaguchi, D. Voiry, T. Fujita, M. Chen, M. Chhowalla, Photoluminescence from chemically exfoliated MoS_2, Nano Lett. 11 (12) (2011) 5111–5116. doi:10.1021/nl201874w.
URL https://doi.org/10.1021/nl201874w

[54] Y. Zhang, Y. Kuwahara, K. Mori, H. Yamashita, Defect engineering of MoS_2 and its impacts on electrocatalytic and photocatalytic behavior in hydrogen evolution reactions, Chem. Asian J. 14 (2) (2021) 278–285.
URL https://doi.org/10.1002/asia.201801594

[55] J. Bradford, A. Zaganelli, D. Qi, N. Zebardastan, M. Shafiei, J. MacLeod, N. Motta, Substrate-mediated growth of oriented, vertically aligned MoS_2 nanosheets on vicinal and on-axis SiC substrates, Applied Surface Science 552 (2021) 149303.
URL https://www.sciencedirect.com/science/article/pii/S0169433221003792

[56] R. S. C. Smart, W. M. Skinner, A. R. Gerson, XPS of sulphide mineral surfaces: metal-deficient, polysulphides, defects and elemental sulphur, Surf. Interface Anal. 28 (1) (1999) 101–105. doi:10.1002/(SICI)1096-9918(199908)28:1<101::AID-SIA627>3.0.CO;2-0.

[57] W. J. Bowman, J. Zhu, R. Sharma, P. A. Crozier, Electrical conductivity and grain boundary composition of Gd-doped and Gd/Pr co-doped ceria, Solid State Ionics 272 (2015) 9–17. doi:https://doi.org/10.1016/j.ssi.2014.12.006.
URL https://www.sciencedirect.com/science/article/pii/S0167273814005141

[58] S. M. Gali, A. Pershin, A. Lherbier, J.-C. Charlier, D. Beljonne, Electronic and transport properties in defective MoS_2: Impact of sulfur vacancies, J. Phys. Chem. C 124 (28) (2020) 15076–15084. doi:10.1021/acs.jpcc.0c04203.
URL https://doi.org/10.1021/acs.jpcc.0c04203